Studying the Potential of Hyperspectral Unmixing for Extracting Composition of Unresolved Space Objects using Simulation Models

Jiarui Yi, Miguel Velez-Reyes, and Hector Erives
Sensor and Signal Analytics Laboratory
Department of Electrical and Computer Engineering,
The University of Texas at El Paso, 500 W University Ave, El Paso, TX, USA 79968
e-mail: jyi2@utep.edu, mvelezreyes@utep.edu, herivescon@utep.edu

ABSTRACT

Space assets are critical for USA defense, security and economic wealth. Remote sensing is an important technology to gain situational awareness of the environment surrounding space assets. Ground-based space telescope technology cannot spatially resolve objects in space that are distant (orbits beyond 1,000 km altitude, e.g. GEO) or that are small (e.g. CubeSats). These objects are denoted as unresolved space objects (URSO). Hyperspectral remote sensing has been proposed as a technology to extract quantitative information about unresolved space objects. The high spectral resolution of hyperspectral sensors contains information about the material composition of the unresolved object from materials' contribution to the measured spectra. Even though the object cannot be spatially resolved, it may be spectrally resolved. Hyperspectral unmixing is a technique used to decompose mixed measured spectral signatures into the spectral signatures of constituent materials and their abundances. In terrestrial applications, unmixing has been widely studied looking at images that contain spectral and spatial information of the object of interest. In the case of unresolved space objects, the authors have proposed the use of the spectro-temporal signature of temporal traces collected while the space object is in transit in the field of view of the hyperspectral sensor to extract material composition information. A big challenge for this approach is that the collected spectro-temporal signature may not be rich enough to extract the material composition using blind hyperspectral unmixing methods. In this paper, we use a simple simulation model of a satellite like object rotating over a background to study how spatial resolution affects the identifiability of URSO material composition. We look at the performance as a function of the spatial resolution in the quality of extracted endmembers and their abundance. Preliminary results show that increase spatial resolution increase identifiability (not a surprising result) but also that few pixels may be sufficient to identify the material composition if the spectro-temporal signature is rich enough.

Keywords: Unresolved Space Object; Hyperspectral Unmixing; Spectro-temporal Signatures; Space Domain Awareness.

1. INTRODUCTION

United States is dependent economically and militarily on space assets [1, 2]. Orbiting satellites provide a multitude of services, which are critical for US's military dominance and economic wealth. Space domain awareness (SDA) is needed to have a clear picture of the environment surrounding US and allied space assets to detect any changes or potential threats. Remote sensing is a key technology for SDA. Remote sensing data for SDA comes primarily from radar and optical systems [3]. Current ground-based space telescope technology cannot spatially resolve objects in space that are distant (e.g., GEO or XGEO) or that are small (e.g., CubeSats, Parasite Satellites). Radar is primarily used for observing targets in LEO while optical ground assets are used to assess the environment at higher orbits.

Current state of the art in optical remote sensing for SDA uses photometric light curves, which show the intensity of light radiated by an URSO over time observed in a specific viewing geometry. Its temporal variability is due to the superposition of shape, attitude, motion, and material composition of an object under a specific viewing and illumination geometry [4]. Multispectral observations (or color photometry) with defined standard sets of passbands provide multispectral light curve observations used for multispectral analysis [5].

Hyperspectral remote sensor such as SPICA [6]or SpeX [7] collect spectroscopic observations of space objects over

a specific period of time. As the object rotates or tumbles different faces of the unresolved space objects are in the field of view of the sensor. The signature on each pixel of the trace is a mixture of the signatures of the materials in the field of view of the sensor at that instant of time. Spectral characterization of materials in space objects and hyperspectral remote sensing for SDA are further described in [8, 9, 10, 11, 12, 13, 14].

The high spectral resolution of hyperspectral systems (HSI) may allow resolving unresolved space objects (URSO) spectrally even though they cannot be spatially resolved. Hyperspectral unmixing is a technique used to decompose mixed measured spectral signatures into the spectral signatures of constituent materials (called endmembers) and their abundances in the field of view of the sensor. It can potentially be used to extract quantitative material composition information about URSOs. In terrestrial applications of HSI, unmixing has been widely studied looking at images that contain spectral and spatial information of the object of interest [15, 16]. In the case of an URSO, however, there are few pixels in the image containing information about the space object so spatial domain information alone cannot be used for unmixing. However, the temporal information of how the measured spectral signature changes as a function of time may be explored to perform unmixing. Figure 1 illustrates the proposed concept. The hyperspectral sensor collects the object signature as a function of time (or spectro-temporal signature), which is used by an unmixing algorithm to extract the material composition of the URSO. The spectro-temporal signature is a vector-valued light curve richer in information than traditional light curves or multispectral light curves described previously. In general, the object spectro-temporal signature can be translated by exploitation algorithms into intelligence for SDA.

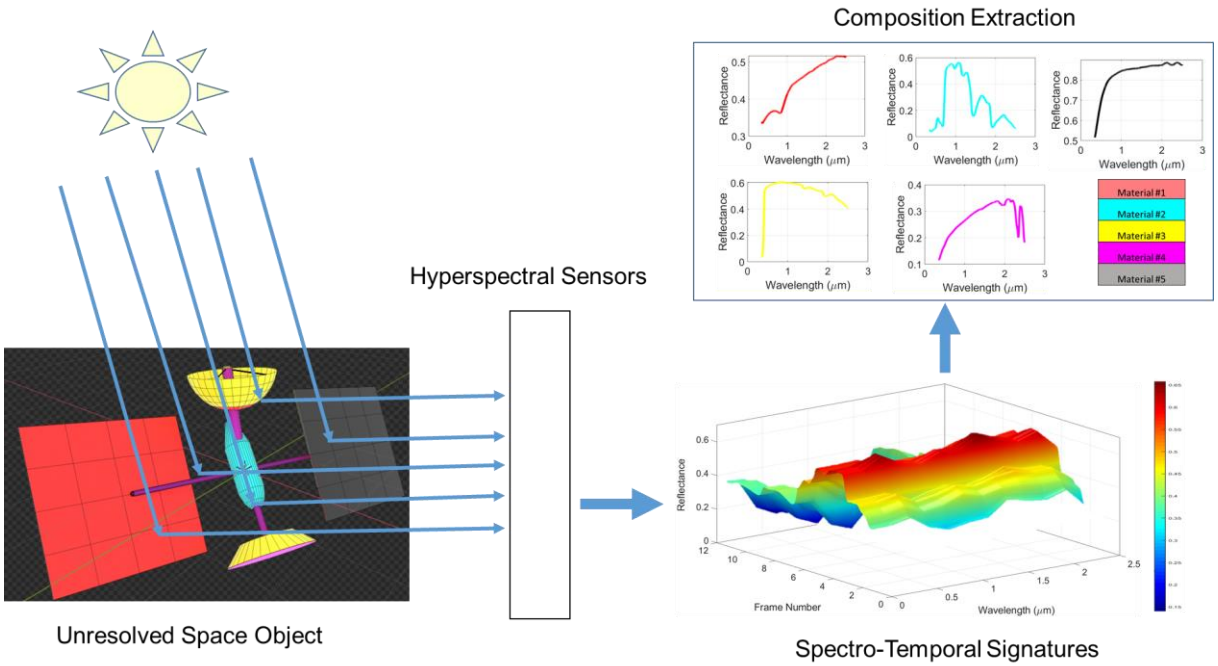

Figure 1. Composition extraction for unresolved space object using hyperspectral unmixing.

In traditional terrestrial applications, the endmember identifiability problem, that is the capability of being able to extract the true endmembers using unmixing from the available data, has been studied and can be quite challenging, when dealing with heavily mixed pixels [17, 18], which is the case of URSO as we studied in [19] and aggravated by lack of spatial information. In this paper, we continue the study of the hyperspectral unmixing problem using spectro-temporal signatures and the effect of spatial resolution to study the identifiability problem in extracting material composition for URSO.

The remainder of the paper is organized as follows. Section II briefly introduces the simple simulation model which simulates a rotating satellite-like object made of different materials. Section III is describes unmixing and presents unmixing results at different spatial resolutions. Section V presents conclusion and final remarks.

2. METHODOLOGY

2.1 Simple Simulation Model for Unresolved Space Object

A simplified simulation scenario was proposed in [20] to generate spectro-temporal signatures to test and validate algorithms for unmixing analysis that can be applied to unmixing of URSO. The scenario consists of the video of a sphere made of patches of different materials rotating at a constant speed over a background. As the ball rotates, different facets of the ball appear in the field of view of the sensor. In [20], mixed signatures were generated by assigning a spectral signature to each color, assuming that each frame was a pixel, and computing the mixed signature using the linear mixing model where each color is associated to a spectral signature and its abundance is equal to the fraction of video frame pixels belonging to that color. The simulation limitations included a symmetric model and which led to a constant fraction of background pixels and we assume that one frame is equal to one pixel. In [20], we showed that the materials were not identifiable and that partial knowledge may slightly mitigate the identifiability problem.

In this study, to be more realistic, we modeled an asymmetric satellite-like simulated object that rotates and tumbles over the background, as shown in Figure 2. The satellite-like object will be the URSO and the background represents the open space. We can see that the amount of background area in the frame varies at different time frames. The spectro-temporal trace will be generated in a similar way as for the patched ball in [20]. Mixed signatures will be generated by assigning a spectral signature to each color, and computing the mixed signature using the linear mixing model where each color is associated to a spectral signature and its abundance corresponds to the fraction of video frame pixels belonging to that color. We will also study different spatial discretization of the video frame to simulate varying spatial resolution as one pixel per frame (same as [20]), a 2×2 grid (4 pixels per frame), and a 4×4 grid (16 pixels per frame) as shown in Figure 3.

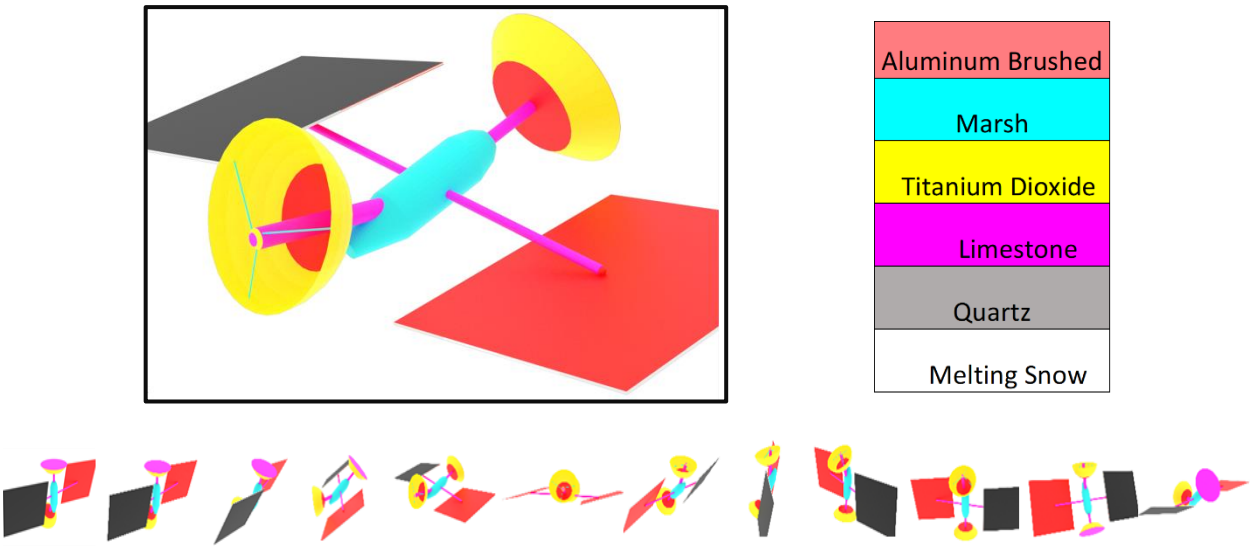

Figure 2. A satellite-like object with varying background area.

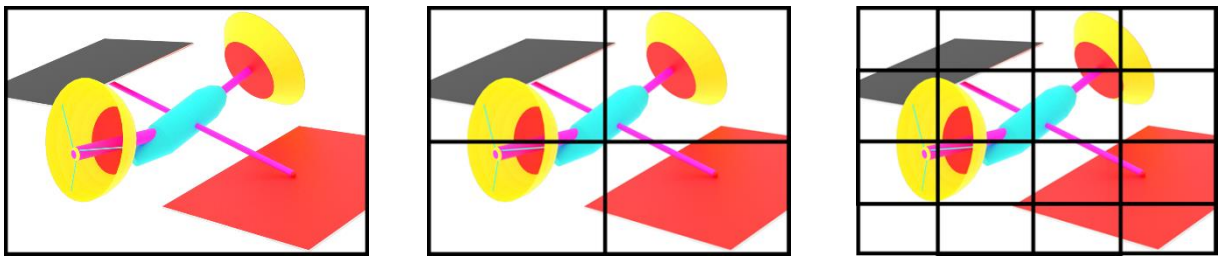

Figure 3. Spatial discretization of the video frame as one pixel per frame, a 2×2 grid (4 pixels per frame), and a 4×4 grid (16 pixels per frame).

Table 1. Abundance for each material at each video frame for the satellite-like object.

Material \ Frame No.	1	2	3	4	5	6	7	8	9	10	11	12
Aluminum Brushed	0.1039	0.0980	0.0278	0.0727	0.1038	0.0391	0.0850	0.0148	0.1169	0.2236	0.2676	0.0205
Marsh	0.0254	0.0247	0.0090	0.0263	0.0253	0	0.0183	0.0139	0.0261	0.0201	0.0251	0.0132
Titanium Dioxide	0.0243	0.0196	0.0109	0.0445	0.0803	0.0744	0.0834	0.0575	0.0708	0.0796	0.0469	0.0320
Lime Stone	0.0390	0.0431	0.0448	0.0232	0.0155	0.0090	0.0145	0.0055	0.0128	0.0147	0.0287	0.0865
Quartz	0.2219	0.1981	0.0879	0.0140	0.0421	0	0.0130	0.0541	0.1158	0.0638	0.0650	0.0349
Melting Snow	0.5855	0.6165	0.8195	0.8193	0.7329	0.8765	0.7858	0.8541	0.6576	0.5982	0.5666	0.8129

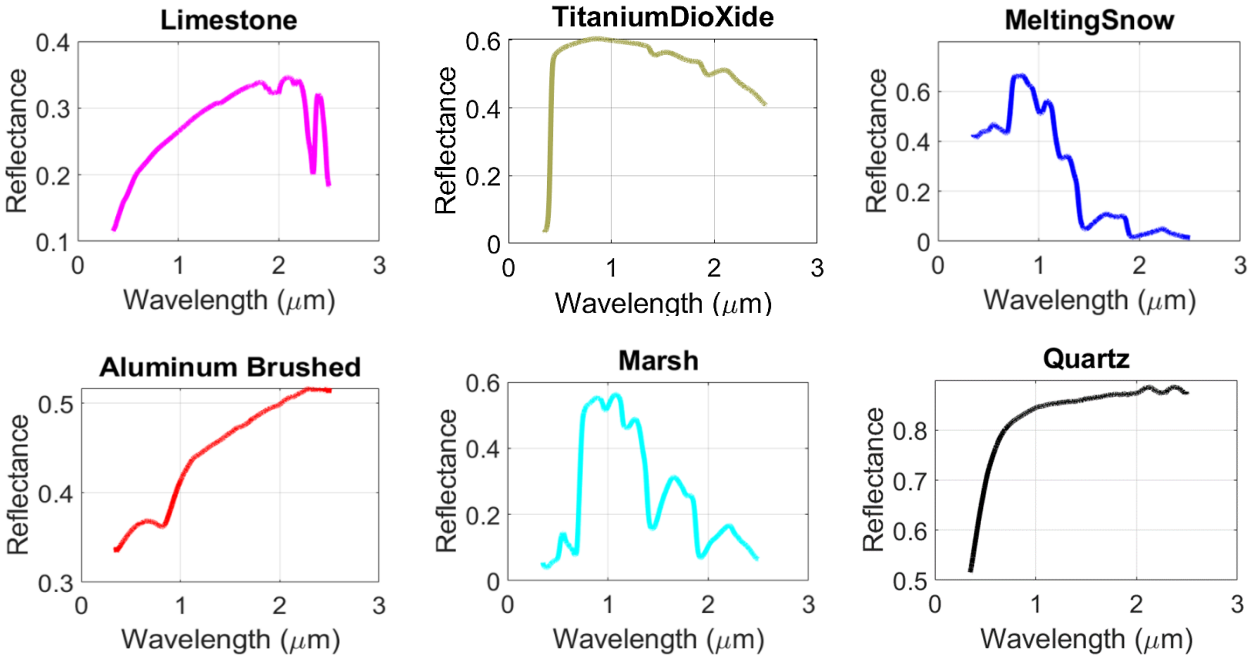

Figure 4. Spectral endmembers used in the simulations [21].

2.2 Simulated Spectro-Temporal Hyperspectral Signatures

Access to hyperspectral telescope data of unresolved object for this project has been challenging because it is not publicly available. The simulation model was created to provide some of the expected spectro-temporal variability of actual hyperspectral measurements to explore and validate the efficacy of unsupervised unmixing algorithms for this application with these simple scenarios. In this study, the satellite object is made of six materials. Signatures for the satellite materials and background (white) were obtained from the USGS spectral library [21] and were assigned to each color as follows: Melting Snow (white-background), Lime Stone (magenta), Titanium Dioxide (yellow), Aluminum Brushed (red), Marsh (cyan), and Quartz (black). The corresponding spectral signatures are shown in Figure 4. We did not used signatures of typical satellite materials but that is not critical for what we want to illustrate. A twelve frames video is generated for this experiment and are shown in the bottom of Figure 2. Table 1 shows the abundance for each material at each full frame. Each column in the table corresponds to the material abundances for

a particular video frame. Each row presents the temporal variation of the abundance for a specific material, and the corresponding images on top shows the corresponding video frame. The number of bands for these spectral signatures used in this study is 2150.

The video frame is spatially discretized as shown in Figure 3. For each spatial pixel, the corresponding mixed spectral signature at each time frame is generated by applying the linear mixing model where the abundance of the materials corresponds to the fraction of video pixels in the spatial pixel belonging to the color associated to the material. One mixed spectral signature is generated for each spatial pixel on each video frame. Figure 5 shows an example of the mixed spectro-temporal signature for the one pixel per frame case. We can think of the spectro-temporal signature as a vector-valued light curve. As an alternate visualization, we can take a top view of Figure 5 which appears as a 2D image shown in Figure 6.

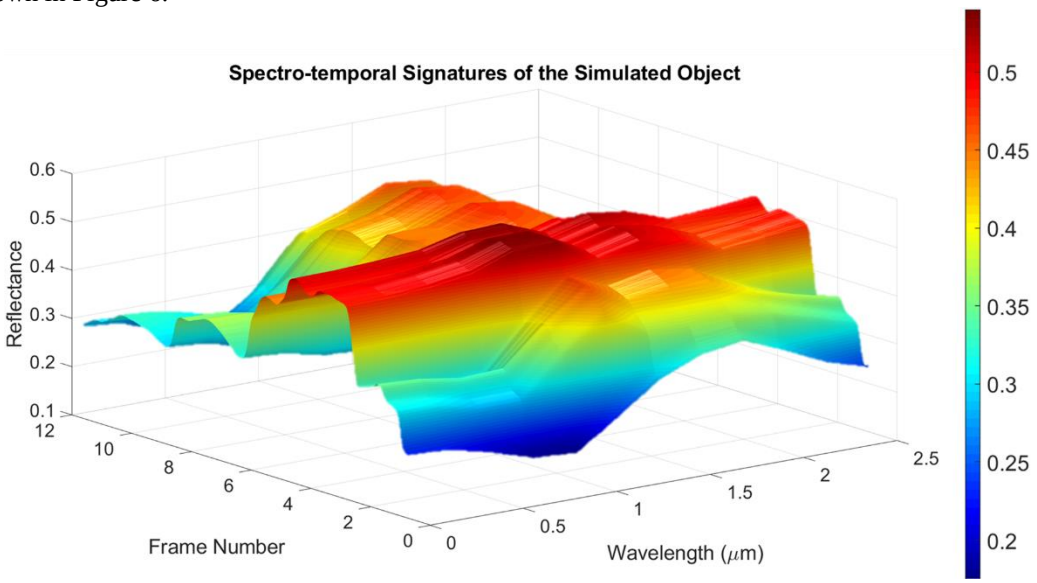

Figure 5. Spectro-temporal signatures of the satellite-like object.

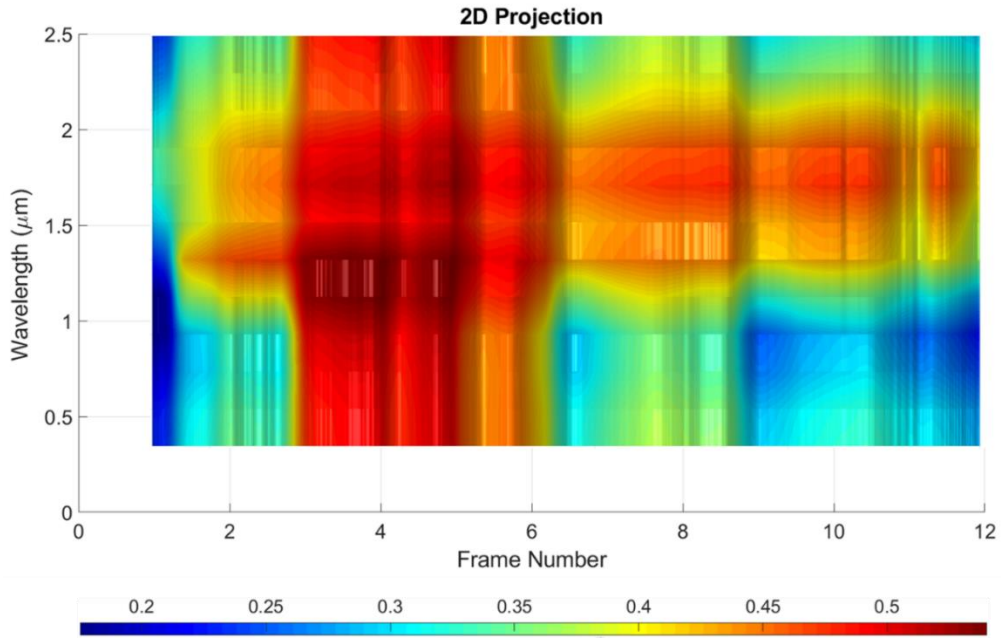

Figure 6. 2D Visualization of the spectro-temporal signature.

2.3 cNMF Unsupervised Unmixing Algorithm

The spectro-temporal signatures of the spatial pixels will be organized into a matrix to take advantage of matrix-based algorithms for unmixing such as the cNMF [22] to perform unmixing. The measured spectro-temporal signature collected during an observation time interval can be organized in a matrix as follows:

$$\boldsymbol{X} = [\boldsymbol{X}_1 \quad \boldsymbol{X}_2 \quad \cdots \quad \boldsymbol{X}_N] \in \mathfrak{R}_+^{m \times qN} \tag{1}$$

where $\boldsymbol{X}_i$ refers to the collection of mixed signatures in the i-th frame, m is the number of bands, N is the number of video frames, and q is the number of pixels per frame (1, 4, or 16). The collection of spectral signatures in the spectro-temporal signatures of all the spatial pixels could be exploited by unmixing procedures to extract material composition information that can be used for object tracking and identification in SSA [19].

In this matrix format, the linear mixing model takes the form of

$$\boldsymbol{X} = \boldsymbol{SA} + \boldsymbol{W} \tag{2}$$

where $\boldsymbol{S} = [\boldsymbol{s}_1 \quad \boldsymbol{s}_2 \quad \cdots \quad \boldsymbol{s}_p] \in \mathfrak{R}_+^{m \times p}$ is the matrix of spectral signatures of the URSO material (endmembers), $\boldsymbol{A} \in \mathfrak{R}_+^{p \times qN}$ is the matrix of abundances, p is the number of endmembers, and $\boldsymbol{W} \in \mathfrak{R}_+^{m \times qN}$ is the noise matrix. Matrices $\boldsymbol{A}$ and $\boldsymbol{W}$ are partitioned commensurate with (1).

The constrained non-negative matrix factorization (cNMF) has been used for unsupervised unmixing of hyperspectral imagery [22]. The algorithm can be summarized as follows. Let $\boldsymbol{X} \in \mathcal{R}_+^{m \times N}$ be the matrix of image pixel spectral signatures like (2) or (3). The cNMF is computed by solving the following optimization problem:

$$\widehat{\boldsymbol{S}}, \widehat{\boldsymbol{A}} = \arg \min_{\substack{\boldsymbol{S} \geq 0, \ \mathbf{A} \geq 0 \\ \mathbf{A}^{\mathrm{T}}\mathbf{1}=\mathbf{1}}} \| \boldsymbol{X} - \boldsymbol{SA} \|_F^2 \tag{3}$$

where $\mathbf{S} \in \mathcal{R}_+^{M \times P}$ is the matrix of endmembers, and $\mathbf{A} \in \mathcal{R}_+^{P \times qN}$ is the matrix of abundances, and p is the pre-determined number of endmembers. In the SSA domain, the availability of spectral libraries of materials such as those from the NASA spectral library [23] and of the space background provide spectral data that can be used as additional constraints in a cNMF-based unmixing. This is not addressed here.

3. EXPERIMENTAL RESULTS

We perform unsupervised unmixing using the cNMF in (3) implemented using an alternate least squares algorithm. Experimental results and comparisons are presented. A twelve frames video sequence of the rotating object is used in the simulation experiment. Each mixed signature was generated for each frame pixel using the linear mixing model as described previously. The cNMF retrieved endmembers are compared to the true endmembers (see Figure 4) using the Euclidean (5) and Cosine distances (6):

$$d_{Euclidean} = \|\boldsymbol{s} - \hat{\boldsymbol{s}}\| = \sqrt{\sum_{i=1}^{m} (s_i - \hat{s}_i)^2} \tag{5}$$

$$\mathrm{d}_{Cosine} = 1 - \frac{|\boldsymbol{s}^T \hat{\boldsymbol{s}}|}{\|\boldsymbol{s}\| \|\hat{\boldsymbol{s}}\|} = 1 - \frac{|\sum_{i=1}^{m} s_i \cdot \hat{s}_i|}{\sqrt{\sum_{i=1}^{m} s_i^2} \sqrt{\sum_{i=1}^{m} \hat{s}_i^2}} \tag{6}$$

where **s** represents the original endmembers, $\hat{\boldsymbol{s}}$ indicates the retrieved endmember. Retrieved endmembers are visually compared to true endmembers in Figure 7 and the corresponding Euclidean (d_1) and Cosine distance (d_2) are shown in Table 2. A not surprising result is that at the number of pixels per tile increases the retrieved signatures are closer to the true ones. With a single pixel per tile only the retrieved background (melting snow) resembles the true signature. With 2×2 grid (4 pixels per frame), background is much closer as well as lime stone, and aluminum brushed, and quartz. For the 4×4 grid (16 pixels per frame), most materials are very close with the exception of Marsh. Note that marsh corresponds to the core body of the space object. Further work is needed to understand how geometrical aspects may affect the identifiability of materials.

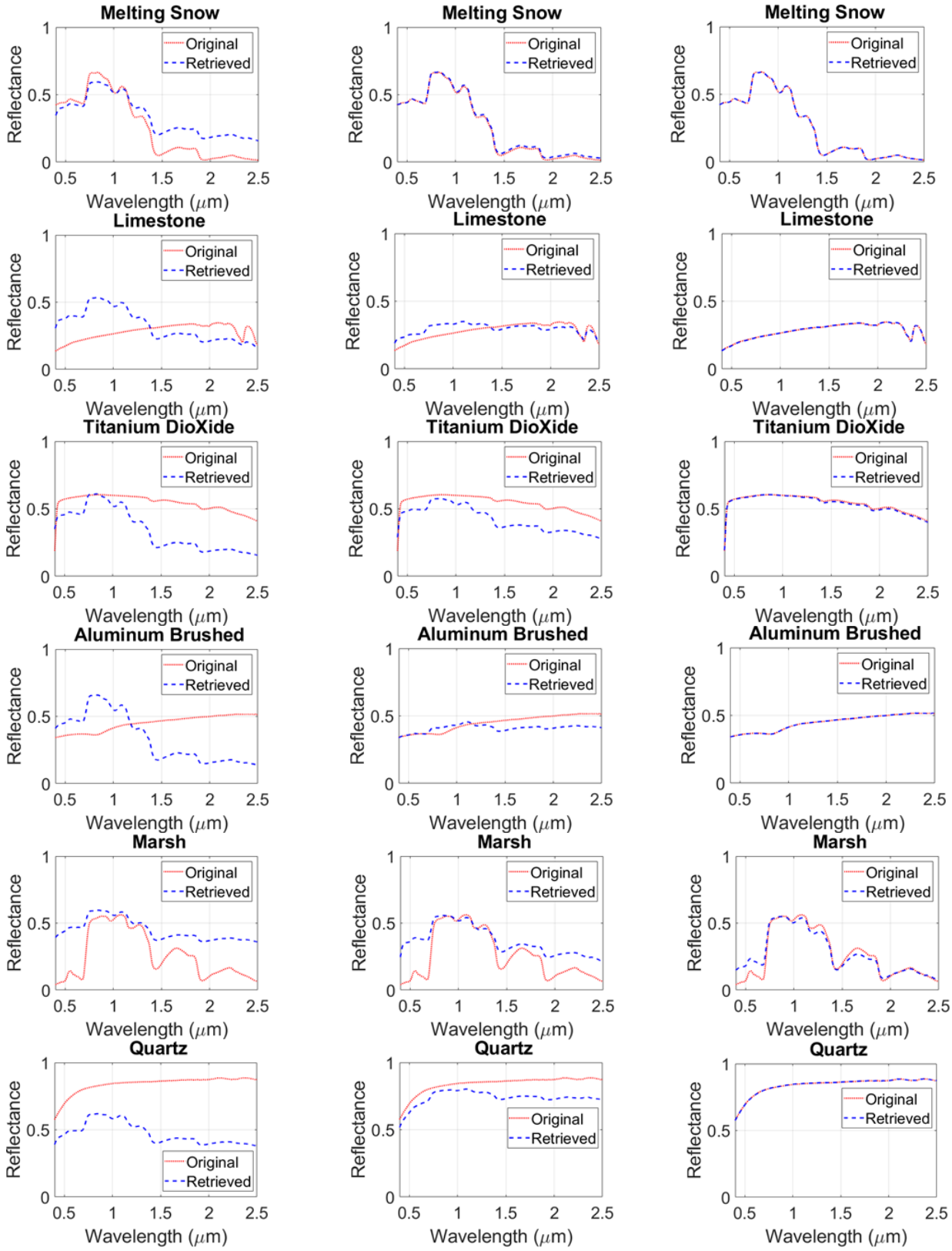

Figure 7. Comparison of endmember retrieved by multiple-tile partitioning: Left column: one pixel per frame; Middle column: 2×2 grid (4 pixels per frame); Right column: 4×4 grid (16 pixels per frame).

Table 2. Distance metrics to evaluate the multiple-tile partitioning.

	Data from USGS Spectroscopy Lab											
	Melting Snow		**Lime Stone**		**Titanium Dioxide**		**Aluminum Brushed**		**Marsh**		**Quartz**	
	d_1	d_2	d_1	d_2	d_1	d_2	d_1	d_2	d_1	d_2	d_1	d_2
1-tile	5.3212	0.0293	7.1951	0.0429	4.6138	0.0109	5.7187	0.0305	6.1845	0.0780	17.6326	0.0183
4-tile	0.5402	0.00045	2.1452	0.0115	6.2727	0.0083	2.8618	0.0058	6.4197	0.0629	4.9827	0.0012
16-tile	0.0115	1.47e-7	0.0561	8.6e-6	0.3596	3.9e-5	0.0269	7.9e-7	2.2341	0.0118	0.0440	5.9e-7

Figure 8 shows 3D scatter plot in principal component coordinates used to visualize the relation between spectro-temporal signatures, retrieved endmembers and true endmembers. The scatter plot shows the mixed signatures as small blue dots, the retrieved endmembers as large red dots, and the true endmembers as large black dots. Figure 8(a) shows the case of one pixel per frame. Clearly the spectro-temporal signature does not fully expand the simplex generated by the true endmembers so the algorithms is not able to retrieve them. As the spatial resolution increases the spectro-temporal signatures fill the simplex more Figures 8(b)-(c) resulting in improved retrievals. Note that the cNMF as an unsupervised algorithm produces endmembers whose simplex encloses the data which is what the algorithms is designed for but is limited by the information contained in the data. This is also reflected in the results shown in Figure 7 and Table 2.

The total abundance for each frame (regardless of the spatial partitioning) are shown in Tables 3-5. The RMSE difference between the true and estimated abundances is included in each Table caption. Comparing them with the ground truth in Table 1 it is clear that better abundance estimates are obtained when the endmembers are closer to the actual endmembers. This is not a surprising result.

4. CONCLUSIONS

An asymmetric satellite-like object was simulated to investigate the identifiability of material composition of unresolved space object using hyperspectral unmixing. Unmixing algorithms were applied to the simulated spectro-temporal signatures of a rotating satellite like object. A data-driven unmixing algorithms based on the constrained non-negative factorization (cNMF) may confront challenges is endmember extraction because of lack of identifiability from the measured spectro-temporal signatures. Experimental results showed that higher spatial resolution, more meaningful spectral endmembers can be extracted. Extracted endmember were closer both in shape (cosine distance) and magnitude (Euclidean distance) as the number of pixels per frame increased. Better endmembers also resulted in better abundance estimates. Interestingly that although all endmember retrievals improved with improved resolution the improvement was not uniform. The endmember associated with the body of the satellite had the highest errors even in the 16 pixels per frame case. This suggest that geometry may play a role in the identifiability of materials for URSO. Future work is looking at developing more realistic simulation scenarios to continue testing and validation of the approach. However, the simple model help to start gaining insight into how hyperspectral technique from terrestrial application may extend to hyperspectral remote sensing for SDA.

5. ACKNOWLEDGEMENTS

This work was supported by the Office of the US Assistant Secretary of Defense for Research and Engineering through the Research and Education Program for Historically Black Colleges and Universities and Minority-Serving Institutions (HBCU/MI) under Award No. W911NF-19-1-0011. Opinions, interpretations, conclusions, and recommendations are those of the author and are not necessarily endorsed by the Department of Defense.

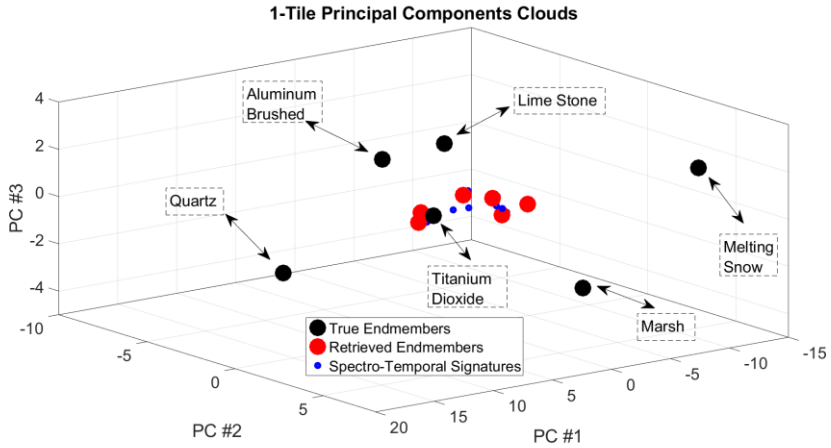

(a)

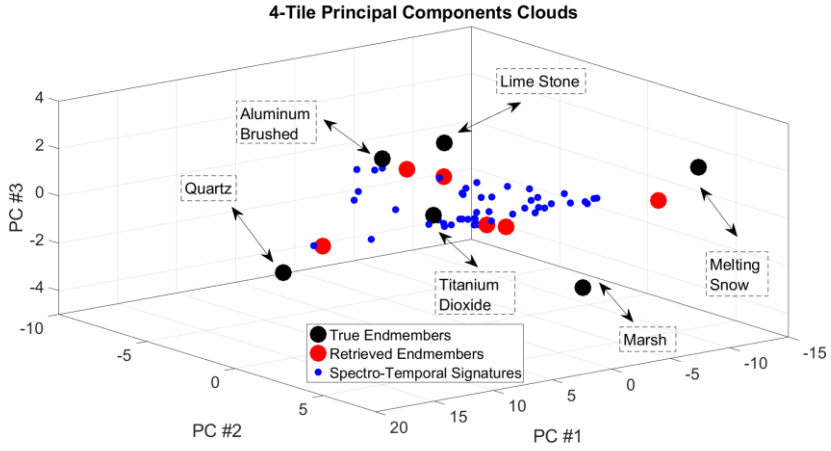

(b)

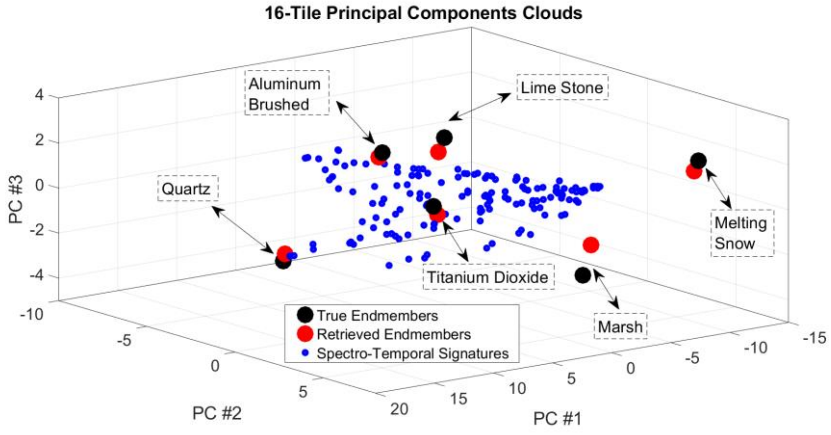

(c)

Figure 8. Visualization of mixed pixels, endmembers, and cNMF retrieved endmembers in 3 principal components coordinates: (a) one pixel per frame, (b) 2×2 grid (4 pixels per frame), (c) 4×4 grid (16 pixels per frame). Mixed signatures as small blue dots, the retrieved endmembers as large red dots, and the true endmembers as large black dots.

Table 3. Abundance estimated by the cNMF algorithm with 1 pixel per tile (RMSE=0.3985).

Material \ Frame No.	1	2	3	4	5	6	7	8	9	10	11	12
Aluminum Brushed	0	0	0	0.0029	0.4405	0	0	0	0	0	0	0.8567
Marsh	0.0037	0.0234	0.0224	0.0005	0.1137	0.9473	0.3935	0.0086	0	0.1350	0	0
Titanium Dioxide	0.0796	0.0109	0.2328	0	0.4416	0	0.0876	0	0.9867	0.3834	0.0881	0
Limestone	0	0.0093	0.6946	0.0673	0	0.0409	0.0461	0.9881	0	0	0.3846	0.0698
Quartz	0.9131	0.9563	0.0500	0.0194	0	0.0090	0	0	0.0132	0.4618	0.5248	0.0516
Melting Snow	0	0	0	0.9017	0	0	0.4726	0.0031	0	0	0.0023	0

Table 4. Abundance estimated by the cNMF algorithm with 4 pixels per tile (RMSE=0.1683).

Material \ Frame No.	1	2	3	4	5	6	7	8	9	10	11	12
Aluminum Brushed	0.2703	0.2793	0.2023	0.0345	0.0923	0.0095	0.0850	0.1097	0.4106	0.3000	0.2376	0.0483
Marsh	0.0463	0.0412	0.0744	0.0046	0.0096	0	0.0850	0.0084	0.1342	0.0699	0.0312	0.2667
Titanium Dioxide	0.0077	0.0023	0.0302	0.0294	0.2210	0.4515	0.2029	0.0509	0.0028	0.0515	0	0.1413
Limestone	0.0722	0.0651	0.0103	0.2959	0.2631	0	0.1123	0.0716	0.0992	0.0968	0.1697	0.1319
Quartz	0.3156	0.2960	0.0408	0.1237	0.1676	0.0426	0.0026	0.0103	0.0516	0.1380	0.1110	0.0204
Melting Snow	0.2831	0.3039	0.6300	0.4955	0.2346	0.4813	0.4946	0.7386	0.2623	0.2927	0.4240	0.3630

Table 5. Abundance estimated by the cNMF algorithm with 16 pixel per tile (RMSE=0.1303).

Material \ Frame No.	1	2	3	4	5	6	7	8	9	10	11	12
Aluminum Brushed	0.1108	0.1056	0.0389	0.1279	0.1199	0.0040	0.0811	0.0602	0.1009	0.0931	0.1156	0.0592
Marsh	0.0307	0.0268	0.0518	0.0418	0.0391	0.0239	0.0388	0.0088	0.0420	0.0302	0.0293	0.2484
Titanium Dioxide	0.2288	0.2260	0.1628	0.0362	0.0791	0.0005	0.0474	0.1016	0.2763	0.1883	0.1998	0.0412
Limestone	0.0185	0.0218	0.0348	0.0990	0.1772	0.2368	0.1489	0.0335	0.0587	0.0727	0.0048	0.1021
Quartz	0.2636	0.2571	0.0525	0.1203	0.1942	0.1032	0.1043	0.0340	0.1864	0.2396	0.1537	0.0645
Melting Snow	0.3471	0.3621	0.6581	0.5722	0.3890	0.6308	0.5788	0.7612	0.3351	0.3746	0.4946	0.4828

6. REFERENCES

[1] M. A. Baird, "Maintaining space situational awareness and taking it to the next level," *Air and Space Power Journal,* 2013.

[2] J. W. Crockett, "Space Warfare in the Here and Now: The Rules of Engagement for U.S. Weaponized Satellites in the Current Legal Space Regime," *Journal of Airlaw and Commerce,* vol. 77, 2012.

[3] S. Eves, Space Traffic Control, vol. 251, T. C. Liewen, Ed., American Institute of Aeronautics and Astronautics, Inc., 2017.

[4] C. Fruh and T. Schildknecht, "Analysis of observed and simulated light curves of space debris," in *Proceedings of the international Astronautical Congress*, 2010.

[5] T. E. Payne and S. A. Gregory, "Passive radiometric observations of geosynchronous satellites," in *2004 IEEE Aerospace Conference Proceedings (IEEE Cat. No.04TH8720)*.

[6] D. L. Nishimoto, J. L. Africano, P. F. Sydney, K. M. Hamada, V. S. Hoo, P. W. Kervin and E. G. Stansbery, "$\less$title$\greater$Spectroscopic observations of space objects and phenomena using Spica and Kala at {AMOS}$\less$/title$\greater$," in *Multifrequency Electronic/Photonic Devices and Systems for Dual-Use Applications*, 2001.

[7] J. T. Rayner, D. W. Toomey, P. M. Onaka, A. J. Denault, W. E. Stahlberger, W. D. Vacca, M. C. Cushing and S. Wang, "SpeX: a medium-resolution 0.8–5.5 micron spectrograph and imager for the NASA infrared telescope facility," *Publications of the Astronomical Society of the Pacific,* vol. 115, p. 362, 2003.

[8] K. J. Abercromby, P. Abell and E. Barker, "Reflectance Spectra Comparison of Orbital Debris, Intact Spacecraft, and Intact Rocket Bodies in the GEO Regime," in *Proceedings of the Fifth European Conference on Space Debris*, 2009.

[9] T. F. Blake, M. E. Goda, S. C. Cain and K. J. Jerkatis, "Enhancing the resolution of spectral images," in *Proceedings of SPIE, Algorithms and Technologies for Multispectral, Hyperspectral, and Ultraspectral Imagery XII*, 2006.

[10] S. Lederer, B. Buckalew, P. Anz-meador, H. Cowardin, J. Frith and M. Matney, "NASA's Ground-Based Observing Campaigns of Rocket Bodies with the UKIRT and NASA ES-MCAT Telescopes," in *Proceedings of the 7th European Conference on Space Debris*, 2017.

[11] T. F. Blake, *Reconstructing Spectral Scenes using Statistical Estimation to Enhance Space Situational Awareness*, Doctoral Dissertation, Air Force Institute of Technology, 2006.

[12] D. Bédard, G. A. Wade and K. Abercromby, "Laboratory Characterization of Homogeneous Spacecraft Materials," *Journal of Spacecraft and Rockets,* vol. 52, p. 1038–1056, July 2015.

[13] S. M. Lederer, J. M. Frith, H. M. Cowardin and B. Buckalew, "NASA Newest Orbital Debris Ground-based Telescope Asset: UKIRT," in *Advanced Maui Optical and Space Surveillance Technologies Conference Proceedings*, 2014.

[14] F. Li, M. K. Ng and R. J. Plemmons, "Coupled segmentation and denoising/deblurring models for hyperspectral material identification," *Numerical Linear Algebra with Applications,* vol. 19, p. 153–173, September 2010.

[15] N. Keshava and J. F. Mustard, "Spectral unmixing," *IEEE Signal Processing Magazine,* vol. 19, p. 44–57, 2002.

[16] J. M. Bioucas-Dias, A. Plaza, N. Dobigeon, M. Parente, Q. Du, P. Gader and J. Chanussot, "Hyperspectral Unmixing Overview: Geometrical, Statistical, and Sparse Regression-Based Approaches," *IEEE Journal of Selected Topics in Applied Earth Observations and Remote Sensing,* vol. 5, p. 354–379, April 2012.

[17] A. Santos-Garcia and M. Velez-Reyes, "Identifiability of geometric models for linear unmixing at different spatial resolutions in hyperspectral unmixing," in *Proceedings of the 2nd IEEE Workshop on Hyperspectral Image and Signal Processing: Evolution in Remote Sensing (WHISPER)*, 2010.

[18] C.-H. Lin, W.-K. Ma, W.-C. Li, C.-Y. Chi and A. Ambikapathi, "Identifiability of the Simplex Volume Minimization Criterion for Blind Hyperspectral Unmixing: The No-Pure-Pixel Case," *IEEE Transactions on Geoscience and Remote Sensing,* vol. 53, p. 5530–5546, October 2015.

[19] M. Velez-Reyes and J. Yi, "Hyperspectral Unmixing for Remote Sensing of Unresolved Objects," in *Advanced Maui Optical and Space Surveillance Technologies Conference Proceedings*, 2020.

[20] J. Yi and M. Velez-Reyes, "Simplified simulation of unresolved objects in hyperspectral remote sensing for space situational awareness," in *Proceedings of SPIE, Algorithms, Technologies, and Applications for Multispectral and Hyperspectral Imagery XXVI*, 2020.

[21] USGS, "Spectroscopy Laboratory," [Online]. Available: https://www.usgs.gov/labs/spec-lab.

[22] Y. M. Masalmah and M. Veléz-Reyes, "A full algorithm to compute the constrained positive matrix factorization and its application in unsupervised unmixing of hyperspectral imagery," in *Proceedings of SPIE, Algorithms and Technologies for Multispectral, Hyperspectral, and Ultraspectral Imagery XIV*, 2008.

[23] H. Cowardin, S. M. Lederer, G. Stansbery, P. Seitzer, B. Buckalew, K. Abercromby and E. Barker, "NASA's Optical Measurement Program," in *Advanced Maui Optical and Space Surveillance Technologies Conference Proceedings*, 2004.